Contents lists available at ScienceDirect

Solar Energy Materials & Solar Cells

Development of W–SiO$_2$ and Nb–TiO$_2$ solar absorber coatings for combined heat and power systems at intermediate operation temperatures

Ewa Wäckelgård [a,*], Andreas Mattsson [a], Ruben Bartali [b], Riccardo Gerosa [c], Gloria Gottardi [b], Fredrik Gustavsson [a], Nadhira Laidani [b], Victor Micheli [b], Daniel Primetzhofer [d], Barbara Rivolta [c]

[a] Solid State Physics, Department of Engineering Sciences, Uppsala University, Uppsala, Sweden
[b] Plasma, Advanced Materials & Surface Engineering, Center for Materials and Microsystems, Fondazione Bruno Kessler, Trento, Italy
[c] Dipartimento di Meccanica, Politecnico di Milano, Milan, Italy
[d] Ion Physics, Department of Physics and Astronomy, Uppsala University, Uppsala, Sweden

ARTICLE INFO

ABSTRACT

Two new absorber coatings for mid-temperature operation (300–350 °C) in collectors for solar thermal electricity plants are presented in this study. The absorbers consist of two cermet layers of either W–SiO$_2$ or Nb–TiO$_2$, deposited on a molybdenum infrared reflector and coated with an antireflection layer of silicon oxide. The optimization of the optical performance was made in two steps. First, the layer structure was optimized in model calculations. The optical constants used in this modelling were derived directly from sputtered films of the cermet constituents using reflectance and transmittance measurements. The absorber coatings were then sputter-deposited using parameters from the modelling. The results show good agreement between modelled and sputtered optical performance evaluated as solar absorptance and thermal emittance at 350 °C. The optimal values reached for W–SiO$_2$ was 0.91 in combination with 0.08 and 0.93 in combination with 0.09 for Nb–TiO$_2$. The materials characterization from XRD, AES and TEM shows that the composite coatings contain nano-metal inclusions, meaning that they are cermet coatings. Scratch tests show that the coatings adhere well to the substrate of stainless steel. Temperature testing at 350 °C in vacuum for up to 1500 h shows that both coatings are stable under such conditions. Only a slight change occurs during the first 72 h that decreases the emittance but does not change the solar absorptance. ERDA confirms that there is no detectable level of ion migration between layers, only a small decrease in hydrogen content was observed, which indicates outgassing.

1. Introduction

Development of absorbers for photo-thermal conversion has in the last years turned more towards applications for electricity generation. Large solar thermal electricity (STE) plants are built in Spain and a number of plants are at present being prospected in sunny areas all over the world. At the same time the STE technique is also developed for small, distributed systems for the domestic sector. We here present the results from a project in which an absorber is being developed for intermediate temperatures (300–350 °C) to be used in a solar concentration system (concentration factor 12) for combined heat and electricity production using a Stirling engine [1].

The renewed interest for STE has resulted in research for new solar absorbers for intermediate and high temperature applications to be used in vacuum collectors with an optically high performing spectrally selective solar absorbing coating on steel tube absorbers. The commercial type of coating used for these applications has since the first STE plants in the 1980th been a cermet (ceramic-metal) composite of Mo–Al$_2$O$_3$ [2]. This type of coating has recently been improved by replacing the infrared reflector coating with silver, stabilized with thin silicon dioxide layers on both sides to prevent degradation [3]. The emittance at 380 °C could then be lowered from 0.13 to 0.06, but in combination with a solar absorptance that decreased from 0.96 to 0.94. Also earlier studies show that silver is a good candidate for reducing thermal emittance but needs a diffusion barrier of a thin dielectric layer between the substrate metal and the silver [4]. There are also some new coatings reported for STE applications that show high solar absorptance in combination with low thermal

* Corresponding author. Tel.: +46 701679101.
E-mail address: ewa.wackelgard@angstrom.uu.se (E. Wäckelgård).

emittance. To these belongs a W–Al$_2$O$_3$ coating with a solar absorptance of 0.94 and thermal emittance of 0.10 at 400 °C [5]. The coating is made by sputter-deposition and is reported to be stable in vacuum during a 30-days test at 580 °C. A recent study of Mo–SiO$_2$ presents a solar absorptance of 0.95 in combination with thermal emittance of 0.15 (400 °C) [6]. Mo–Al$_2$O$_3$, W–Al$_2$O$_3$ and Mo–SiO$_2$ absorber coatings referred to above consist of three sub-layers for solar absorption (see Fig. 1): a base cermet layer of higher metal content on the infrared reflector, an intermediate cermet layer with a lower metal content and on top, an antireflection coating of a pure dielectric material. This is a well-known concept used in many cermet-based absorbers for low-temperature applications and utilizes absorption in the metal nano-particles and reflectance suppression with thin film optical interference. A new different type of coating design based on a-periodic multiple metallic-dielectric alternating layers using Mo or W as metal has been reported [7]. With a four-layer Mo–MgO coating a solar absorptance of 0.94–0.95 and a thermal emittance of 0.06–0.07 (at 450 °C) was achieved in model calculations. Another concept was reported in [8], using laser sintering of W particles on stainless steel to produce a rough surface that enhances the solar absorptance of a tungsten surface from about 0.52–0.83, in combination with a thermal emittance of 0.12 (300 K).

A comprehensive review on mid- to high-temperature solar selective absorber materials is reported by Kennedy [9]. Many of the coatings referred to in this report originally aimed for low temperature applications in ambient atmosphere have been tested at mid-temperatures (100–400 °C) and proved to be stable in air in a range from 200 to 425 °C depending on materials compositions. A few coatings such as black copper, black chrome, and TiNO$_x$ was found to be stable at 370 °C, 400 °C and 400 °C respectively. Kennedy suggests that several of the commercial coatings for low temperatures could be potential candidates also for mid-temperature applications. These candidates are mostly composite cermet types with 3d- or 4f-metals in combinations with oxides, carbides or nitrides and proved in general to be stable at these temperatures.

The main objective of this study is the design of innovative feasible solar absorber coatings with a solar absorptance in the range 0.93–0.95 (or higher if possible) and combined with a thermal emittance at 350 °C between 0.06 and 0.10. Two solar selective coatings are studied, W–SiO$_2$ and Nb–TiO$_2$. Both cermets are composed by low cost, non-toxic and high melting point materials. Previous literature on these cermets is rather scarce. It was found only one study on W–SiO$_2$ presenting theoretical optimizations of one to four sub-layers of W–SiO$_2$ [10]. The solar absorptance obtained in this study was 0.97 in combination with a thermal emittance at 400 K of 0.04. No relevant literature was found on Nb–TiO$_2$. The coating closest in composition was NbTiON [11].

The absorber we develop is a three-layer-absorbing coating (see Fig. 1) on molybdenum infrared reflector deposited on stainless steel. Stainless steel ha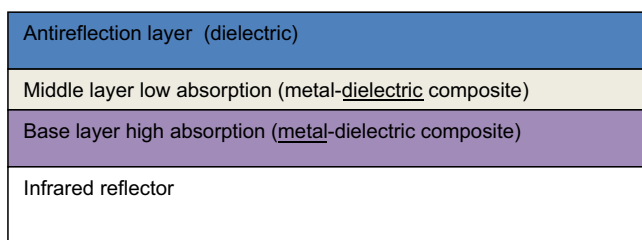s too high infrared reflectance to be used as reflector and the standard solution for mid-temperature absorbers is to deposit a Mo infrared reflector to lower the thermal emittance [2]. The optimization procedure started with sputtering the metal and ceramics in the cermets separately as semi-transparent films on glass to determine their optical constants. The optical constants were used in the first round of parameter optimization by calculations. After that the absorber coatings were sputtered using these optimal parameters and in the final step the process parameters were tuned to obtain the best combination of solar absorptance and thermal emittance (at 350 °C). The absorber coatings were characterized in order to verify cermet structure, layers thickness, possible contamination by other elements and crystal order. The stability of the samples was also tested at 350 °C in vacuum for up to 1500 hours. Optical, structural and mechanical properties were investigated before and after the annealing.

Modelling of the three-layer solar absorber stacks was done with SCOUT software tool for optical simulation and optimization of optical coatings [12]. The programme uses the complex refractive index, for each layer to calculate the reflectivity of the total stack of layers. For the cermet layers the Bruggeman effective medium theory was used to model effective optical constants of the cermets.

The key values for evaluation of solar absorber coatings are the solar absorptance

$$\alpha_{sol} = \frac{\int_{0.3\ \mu m}^{4.1\ \mu m} I_s(\lambda)\alpha(\lambda)d\lambda}{\int_{0.3\ \mu m}^{4\ \mu m} I_s(\lambda)d\lambda} \tag{1a}$$

and thermal emittance

$$\varepsilon_T = \frac{\int_{0.3\ \mu m}^{100\ \mu m} I_{bb}(\lambda)\varepsilon(\lambda)d\lambda}{\int_{0.3\ \mu m}^{100\ \mu m} I_{bb}(\lambda)d\lambda} \tag{1b}$$

Solar absorptance as defined above is the spectral absorptance, $\alpha(\lambda)$, weighted with the solar spectral distribution $I_s(\lambda)$, here using ISO standard 9845-1(1992) for air mass 1.5. Thermal emittance is defined as spectral emittance, $\varepsilon(\lambda)$, weighted with the spectral distribution of blackbody radiation $I_{bb}(\lambda)$, at 350 °C. Spectral absorptance and emittance are derived from $1 - \rho(\lambda)$, where $\rho(\lambda)$ is theoretically calculated spectral reflectance from SCOUT simulations or experimentally measured reflectance on fabricated samples. In the following values for near normal angle of incidence are used in the calculations.

2. Experiment procedures

2.1. Sample fabrication

DC sputtering was used to deposit molybdenum reflectors on the SS substrate. The W–SiO$_2$ cermets were rf sputtered from two targets, tungsten and silicon oxide. The AR-layers were sputtered with the same process as the SiO$_2$ component in the cermet. The Mo, W–SiO$_2$ and SiO$_2$ layers were prepared in a Balzer UTT400 sputtering unit. The working chamber is equipped with a turbo molecular pump TMU 521P. The chamber has a base pressure of 1×10^{-4} Pa after baking. Argon was sprayed into the chamber from a nozzle controlled by a mass flow controller (Bronkhorst Hi-Tec). The pressure in the chamber was adjusted by a manual valve mounted between chamber and pump and was measured by a capacitance diaphragm gauge (model of CMH-01S07). The sample holder was rotated to obtain an even thickness of deposited layers. The Nb–TiO$_2$ cermets were prepared in an on-site constructed sputtering unit at Fondazione Bruno Kessler in Trento. The TiO$_2$ films were deposited by rf plasma sputtering of a titanium oxide target while Nb was deposited by rf magnetron-sputtering. Films were prepared using argon gas (30 sccm) in the pressure range

Fig. 1. Three-layer absorber coatings in cross-sectional view. The numbering from bottom to top is (1) infrared reflector; (2) high-absorbing base layer; (3) low-absorbing intermediate layer; (4) antireflection layer.

Table 1
Sputtering parameters used in the preparation of the most feasible solar absorber coatings. Deposition rate is determined from deposition on glass substrate with same settings.

Coating	Voltage (power)	Base pressure/Ar pressure [Pa]	Ar flow [sccm]	Deposition rate [nm/min]	Deposition time [min]
Mo reflector	495 V (320 W)	$0.3 \times 10^{-3}/0.17$	6.6	14	7.0
W on glass	-252 V bias (71 W)	$0.3 \times 10^{-3}/0.40$	14	2.8	6.5
SiO$_2$ on glass	-800 V bias (332 W)	$0.3 \times 10^{-3}/0.40$	14	3.9	40
W–SiO$_2$ base-layer	-800 V bias (318 W) (SiO$_2$ target) -208 V (53 W) (W target)	$0.3 \times 10^{-3}/0.40$	14	5.4	14
W–SiO$_2$ middle-layer	-800 V (337 W) (SiO$_2$ target) -84 V/10 W bias -80 V (W target)	$0.3 \times 10^{-3}/0.40$	14	3.4	14
Nb on glass	-252 V bias (49 W)	$8 \times 10^{-5}/0.45$	30	6.0	5
TiO$_2$ on glass	-920 V bias	$8 \times 10^{-5}/0.45$	30	0.8	75
Nb–TiO$_2$ base-layer	-890 V (TiO$_2$ target) 45 W (Nb target)	$8 \times 10^{-5}/1.3$	30	9.6	4
Nb–TiO$_2$ middle-layer	-890 V (TiO$_2$ target) 15 W (Nb target)	$8 \times 10^{-5}/1.3$	30	4.5	6.33
SiO$_2$ AR-layer	-560 V (203 W)	$0.3 \times 10^{-3}/0.40$	14	2.7	25

0.4–7×10^{-3} Pa. The samples were deposited at floating potential and were not externally heated. See also all relevant process data in Table 1.

Firstly, a set of samples on Corning glass was sputter-deposited in order to determine the optical constants of the constituents in the cermets: W, Nb, SiO$_2$ and TiO$_2$. The samples were made semi-transparent in order to measure both reflectance and transmittance. Sample thickness for SiO$_2$ and W layers was determined with a Dektak XT stylus profilometer whereas the thickness for TiO$_2$ and Nb layers was determined with a KLA Tencor P15T stylus profilometer. Similar sputtering conditions were used when preparing the oxides on glass and later on in the cermets, and are presented in Table 1.

The substrate was electro-polished stainless steel type AISI302, which was thermally annealed for 1 h in air at 100 °C to remove stress and then cleaned by ethanol in an ultra-sonic bath before deposition. Surface roughness was determined to be 0.3 µm as measured over a 3 mm × 5 mm area with a Bruker Dektak Stylus profilometer equipped with a stylus with a radius of 12.5 µm. The process parameters for sputtering the molybdenum infrared reflector were investigated in detail in order to obtain the highest possible infrared reflectance. The best conditions for high quality sputter-deposited reflectors are low argon pressure and high electric power (i.e. high deposition rate) and a layer thickness that gives a complete coverage of the surface. The lowest possible argon pressure is limited by a functioning magnetron and this limit was about 0.1 Pa for this magnetron. Several power levels were tested and it was found that using powers from 300 W or higher gave the best achievable quality. The coating thickness should be least 100 nm for the actual surface roughness.

2.2. Sample characterization

The main characterization is based on optical measurements of reflectance within the solar wavelength range for calculation of near normal solar absorptance (Eq. (1a)) and the infrared wavelength range to calculate near normal thermal emittance at 350 °C (Eq. (1b)). Additional to this, it was important to investigate structural and mechanical properties before and after tests at operation temperatures. A brief survey of the different measurements techniques used in the study will follow in this chapter.

2.2.1. Optical characterization

A Perkin-Elmer Lambda 900 UV/VIS/NIR double beam spectro-photometer was used for measurements in the solar spectral range from 0.3 to 2.5 µm. The instrument is equipped with an integrating sphere to allow for measurements on optically rough surfaces. As reference an optical-grade Spectralon sample was used. It is characterized by a high reflectance and Lambertian behaviour and is primarily used as a reference standard for spectrophotometers in the UV–vis NIR wavelength range [13]. Measurements were done at near normal angle of incidence. For the films deposited on glass both reflectance and transmittance were measured.

The instrument used for measurements in the infrared wavelength range was a FTIR TENSOR 27 from Bruker. The instrument is equipped with an integrating sphere coated with gold. The measuring wavelength range is from 2.5 to 22 µm. Measurements were done at near normal angle of incidence. According to the standard EN 673, the thermal emittance should be calculated covering at least to 50 µm. The reflectance is therefore assumed to be constant and extrapolated to 100 µm by using the average reflectance of the five measured data points at longest wavelengths.

Optical constants for sputter deposited thin films of tungsten, niobium, silica and titania were determined from reflectance and transmittance measurements in the 0.3–2.5 µm range on semi-transparent films using SCOUT. For each of the films the thickness is determined with a profilometer and in SCOUT a model was created and fitted to the measured data. During this procedure the measured thickness is allowed to vary by 10%. The optical properties for the glass substrate were first determined independently using the same method and also showed good comparison with the reference supplied with the software. From these models of the pure films the optical constants, n and k, could then be retrieved.

2.2.2. Electron microscopy

Transmission electron microscopy (TEM), was used to investigate morphology, layer thickness, metallic phase (if present), crystallite size, difference (if present) between as-deposit and annealed samples.

TEM cross sections were prepared using in situ lift-out in a FEI Strata D235 Focused Ion Beam (FIB) instrument, using 30 keV Ga ions. To avoid ion beam damage of the top surface, a thin metal-organic Pt layer is initially deposited by first using the electron beam, then the ion beam. To further minimize the beam damage, only 5 keV ion beam energy was used in the final steps of the sample preparation. The sample thickness varies between 30 and 100 nm. TEM analysis was performed at 300 kV acceleration

voltage using a FEI Tecnai F30 ST microscope, equipped with a Gatan post column energy filter.

2.2.3. Auger electron spectroscopy

AES analyses were carried out using a Physical Electronics model 4200 system, equipped with a variable resolution cylindrical mirror analyser (CMA, $0.3 \pm 1.2\%$) and a coaxial electron gun. W_{NNN}, C_{KLL}, Nb_{MNN} Si_{LMM} Ti_{LMM}, Ti_{LMV} and O_{KLL} Auger lines were acquired in derivative mode and an elemental quantification applying the manufacturer's relative sensitivity factors has been achieved. Three types of analysis were performed: survey scan spectra of the surface of the as-received samples, survey scan spectra after 1 min of ion etching and multiplex of metal region after 1 min of ion etching. The AES measurements are used to determine whether the metal elements in the cermets (W or Nb) are in metal phase as assumed in the modelling.

2.2.4. X-ray diffraction

Grazing incidence X-ray diffraction was performed with a Siemens D5000 instrument, equipped with a Goebel mirror to filter out the Cu-K$_\alpha$ radiation. For these measurements the films were deposited directly on amorphous glass substrates (Corning glass) to prevent strong signals from the metals in the stainless steel and Mo infrared reflector. XRD was used to determine metal content (W or Nb) and crystal order in the oxides (SiO_2 or TiO_2).

2.2.5. Elastic recoil detection analysis

Time-of-Flight Energy ERDA (ToF-E ERDA) permits to obtain composition and depth profiles of elements in a sample from coincidence measurements of flight time and energy of target ions and atoms recoiled from energetic (heavy) primary ions. The coincidence measurement permits to determine both energy and mass of recoils. ToF-E ERDA experiments were performed at the tandem accelerator laboratory at Uppsala University. Samples were transferred to a vacuum chamber at a base pressure below 1×10^{-4} Pa. 36 MeV $^{127}I^{8+}$ ions were used as primary projectiles. The detection beam line is situated under an angle of $45°$ with respect to the primary beam. Further details on the detection systems see [14–16]. The choice of the primary ion and its energy enables depth profiling of all elements of interest down to a depth of about 200–300 nm, depending on the composition of the target. Energy loss straggling in the sample leads to a depth dependent resolution in the sample, with the highest resolution for smallest energy losses, i.e. close to the surface. Whereas depth resolution below 20 nm can be achieved for light elements, the depth resolution for more heavy species may in certain cases exceed 40 nm if they are situated at large depth. Evaluation of coincidence spectra of recoils is done using the CONTES software package [17].

2.2.6. Scratch test

Scratch tests were performed according to ASTM C 1624-05 Standard both before and after annealing at $350 °C$ under vacuum. According to the standard, tests can be carried out both with constant loads or with increasing loads during the indenter stroke. The indenter is a Rockwell C diamond cone with tip angle and radius equal to $120°$ and $200 \mu m$ respectively. In the present investigation an increasing load technique was employed, according to the following parameters: scratch length was 3 mm, translation speed was 1.25 mm/min and maximum load was 30 N.

2.3. Durability tests

Durability of absorber coatings is crucial for good performance in long time operation. Since the absorbers in this study are aimed for vacuum tube collectors the main degradation mechanism is expected to be temperature related, on submicron scale such as ion migration, change in chemical compositions and outgassing. Also, degradation on microscopic scale such as stress-related changes leading to worse adhesion, cracks and bad surface coverage can occur.

Temperature tests were made in a pipe oven (8 cm diameter, 62 cm long) from ENTECH, Sweden. A gauge metre was installed at one end of the tube chamber and a pressure of 5×10^{-3} Pa could be reached. The samples were placed in a small metallic box ($100 \text{ mm} \times 50 \text{ mm} \times 25 \text{ mm}$) centrally positioned in the oven in order to get comparatively homogeneous temperature. A thermal couple was fixed on an inner surface of the box to monitor the sample temperature, which was $350 °C$. If not indicated the annealing time was first 72 h (3 days), then optical measurement was performed and the test continued up to totally 1500 h and the samples were optically re-measured.

3. Experimental results and discussion

3.1. Optimal coating design

The optical constants for sputtered thin films of the cermet constituents on glass were derived from reflectance and transmittance measurements in the UV–vis–NIR wavelength range on semi-transparent samples as described earlier. Tungsten was modelled with a Drude model and three harmonic oscillators whereas the SiO_2 film was modelled using a dielectric background and three harmonic oscillators. For Nb a Drude model and two harmonic oscillators was used and for TiO_2 three harmonic oscillators in conjunction with an interband transition model.

Fig. 2 shows n and k, fitted from experimental data and from literature for W [18] and Nb [19]. The fitted n and k deviates strongly from literature data for wavelength longer than about $0.7 \mu m$. The extinction coefficient is lower and the refractive index higher for the film optical constants. However the reflectance calculated for an opaque surface using these constants could be similar to the reflectance calculated from literature data since a lower extinction coefficient is compensated by a higher refractive index. The literature data is for bulk metals and show interband transitions that are not present in the experimental optical constants of the same metals as thin films. The experimental data show a simpler free-electron like dispersion relation. The semi-transparent films are indeed very thin (tungsten film thickness 18 nm), which is much thinner than the wavelengths. It is problematic to determine optical constants from reflectance and transmittance data for very thin metal films. A more reliable method is to use Kramer–Kronig relations but in the present context the simpler method used here serves well.

Fitted n (k is zero) for silicon oxide is close to the literature data for amorphous silicon oxide (glass) [18], but slightly higher as seen in Fig. 3a. This can be an artefact and depend on the Corning glass-substrate, which itself has a higher refractive index. The titanium oxide presented in Fig. 3b has a considerably lower n and k than the literature data and shows a decline in absorption for shorter wavelengths. The literature data represents rutile titania (bulk) [18], and the sputtered films have an amorphous structure according to the XRD results (see Section 3.2.3). The peak in n at $0.4 \mu m$ indicates interband transition in the rutile titania which is not present in the sputtered films. The comparison with literature data for bulk solids shows that it is important to use optical constant from the sputtered films instead of literature data in the optimization procedural for optical design of the absorbers.

The optical constant could with this method (semi-transparent films on glass) only be used in the UV–vis–NIR wavelength range. Optical constants for longer wavelengths (2.5–10 μm) were
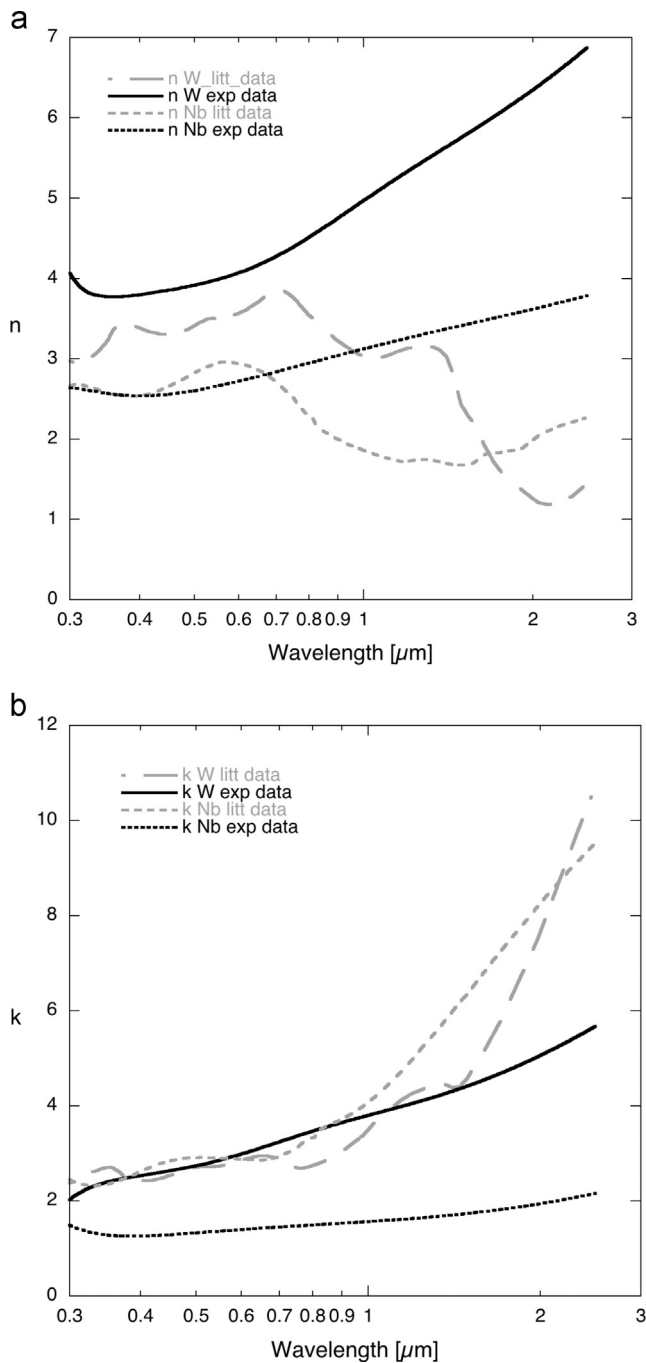
Fig. 2. Fitted optical constants for sputtered cermet constituents, the metal component (a) W and (b) Nb with literature data for comparison [18,19].

Fig. 3. Fitted optical constants for sputtered cermet constituents, (a) the oxide component SiO_2 and (b) TiO_2 with literature data for comparison [18].

extrapolated as constant values using the last NIR values. For the Mo reflector optical constants from literature [18] were used in the calculations.

Fig. 4 shows the reflectance of the modelled and sputtered coatings after depositing base, middle and AR layers in W–SiO_2 absorber. It was not possible to reach exactly the same reflectance as modelled in each layer, which is an effect of the level of accuracy in derived optical constants and in reproducibility in the sputtering process. A consequence of this was then to make a small adjustment in the thickness of each layer to be as close as possible to the model reflectance after each deposition. Fig. 5 shows the reflectance after depositing of both middle and base layer of Nb–TiO_2 (a) and the reflectance after the AR layer deposition (b). The use of bulk optical data for Mo reflectors gives
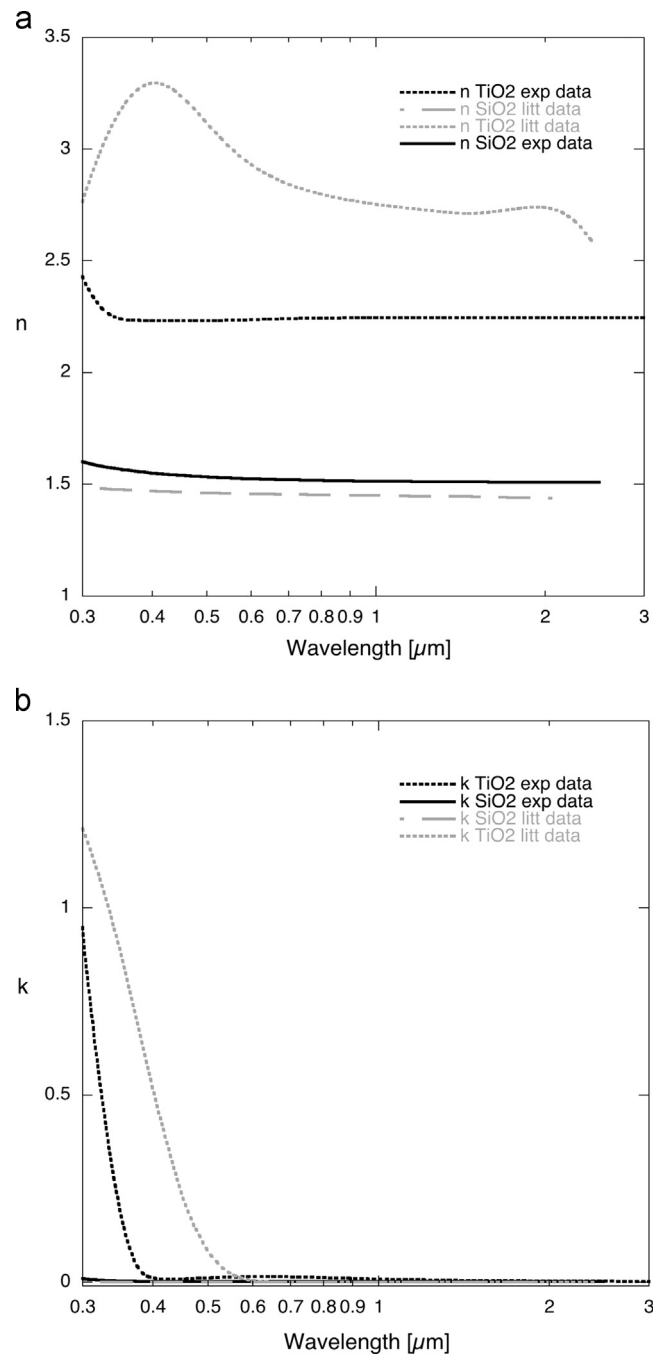
a higher infrared reflectance compared to the real coatings. The reflectance of an ideal Mo is lower (0.05 at 350 °C) but for the deposited films it reached up to 0.07 or 0.08. It is seen in both cermet type absorbers that the final result after depositing all three layers come closest to the model reflectance, which is deliberate strategy in the experimental optimization.

Relevant data such as layers thickness, metal volume fractions, absorptance and emittance are presented in Table 2. For the W–SiO_2 absorber the modelled solar absorptance of 0.93 could not be reached in the as-prepared coatings, which is also clearly seen in Fig. 4c, as an effect of a narrower bandwidth with low reflectance for the sputtered cermet. The layers thickness values are close for the base layers, the sputtered middle layer is 12% thicker and the AR layer is 30% thinner than modelled layers respectively. The total
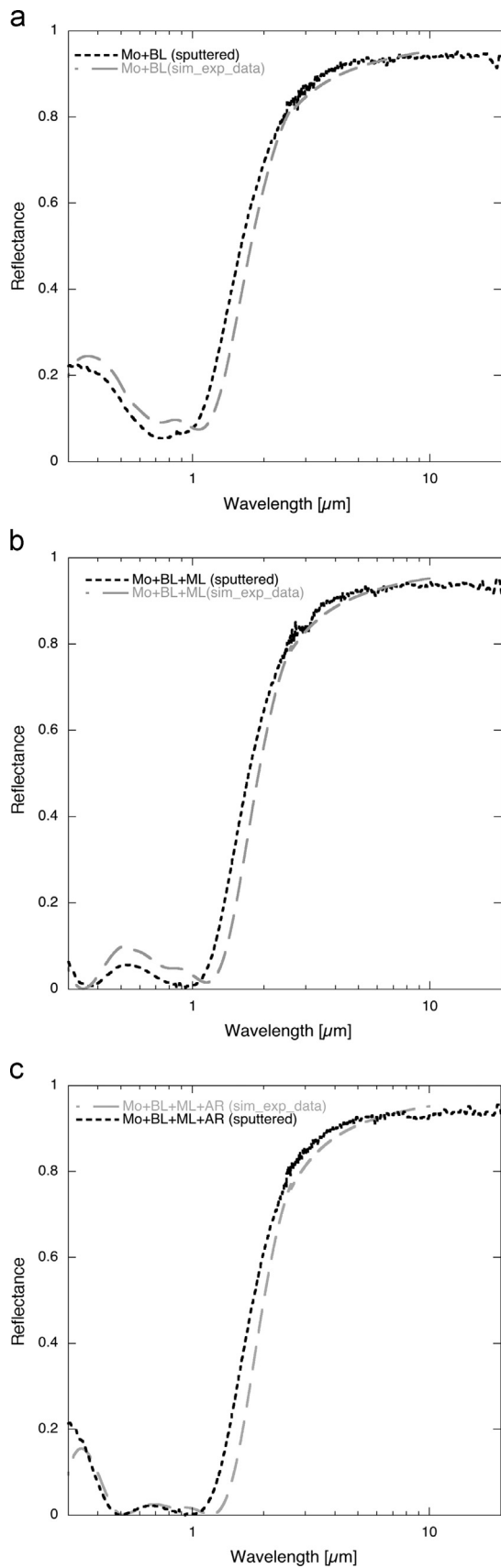
Fig. 4. W–SiO$_2$ optimized solar absorber (a) molybdenum reflector and the W–SiO$_2$ base layer, (b) molybdenum reflector, the W–SiO$_2$ base layer and W–SiO$_2$ middle layer, (c) molybdenum reflector, the W–SiO$_2$ base layer, W–SiO$_2$ middle layer and SiO$_2$ AR layer. Optical constants derived from sputtered films of W and SiO$_2$ are used in the modelled coatings.
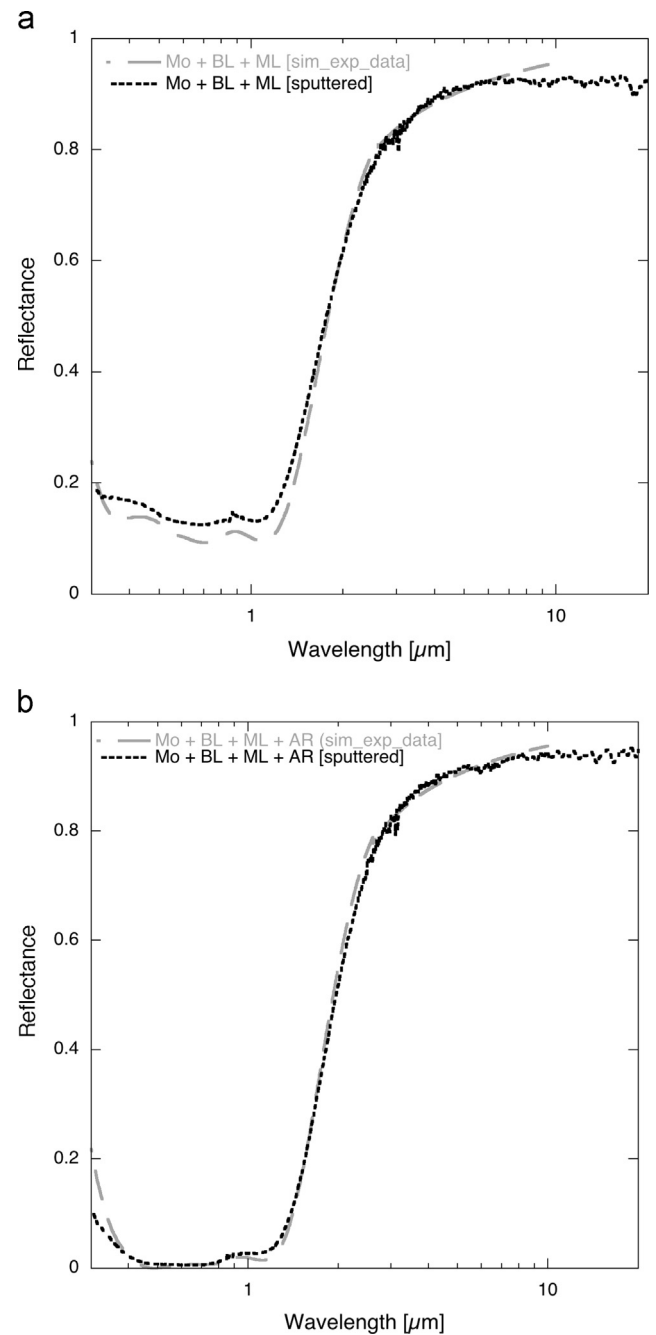

Fig. 5. Nb–TiO$_2$ optimized solar absorber (a) molybdenum reflector, Nb–TiO$_2$ base layer and Nb–TiO$_2$ middle layer, (b) molybdenum reflector, Nb–TiO$_2$ base layer, Nb–TiO$_2$ middle layer and SiO$_2$ AR layer. Optical constants from literature and derived from sputtered films of W and SiO$_2$ are used in the modelled coatings.

absorber coating is 5% thinner in the sputtered than in modelled absorber. The volume fraction of W is very low in the modelled coating. This will be analysed and discussed further in Section 3.2.1.

For the Nb–TiO$_2$ absorber the same solar absorptance and thermal emittance as for the modelled was reached. The spectral reflectance of the sputtered absorber follows the model one very well (Fig. 5b). Here the base layer is about 10% thinner in the sputtered coating, the middle layer has about the same thickness and the AR layer is 14% thinner than the corresponding modelled layers. The total thickness is 9% thinner in the sputtered coating.

These results can be compared to those obtained from simulations using literature data for bulk materials. For the Nb–TiO$_2$ based absorbers the solar absorptance and thermal emittance is

Table 2

Comparison of results from optimization: theoretical using optical constants from sputtered samples, and experimentally, in sputtered coatings. Thicknesses of sputter-deposited coatings are from deposition rates and times in Table 1.

	α_{sol}	$\varepsilon_{350}T$	Layer 1 (cermet)		Layer 2 (cermet)		Layer 3 (AR) t_3 (nm)	Total absorber thickness (nm)
			f_1	t_1 (nm)	f_2	t_2 (nm)		
SiO$_2$/W–SiO$_2$/Mo/SS								
Modelled coating with optical constants from the sputtered films	0.93	0.09	0.33	75	0.08	42	51	168
Sputtered coating	0.91	0.08		76		48	35	159
SiO$_2$/Nb–TiO$_2$/Mo/SS								
Modelled coating with optical constants from the sputtered films	0.93	0.09	0.79	47	0.25	29	79	155
Sputtered coating	0.93	0.09		43		30	68	141

calculated to be 0.92 and 0.09 respectively whereas for the W–SiO$_2$ based structure the solar absorptance and thermal emittance is calculated to be 0.96 and 0.09. The difference in performance between the simulated solar absorber stacks and the realized structures can be found in the discrepancy of the optical constants of the sputtered films and bulk materials, see Fig. 2.

3.2. Structural characterization

The results presented so far in Section 3.1 show that it is possible to optimize absorber coatings using a rather simple method for deriving optical constants from reflectance and transmittance measurements. This method is based on modelling of cermet coatings using effective medium theory, with well-defined metallic particles and oxide matrices surrounding the latter, at least for lower metal concentrations. In the following we report on results that could support a cermet structure in the real sputtered coatings.

3.2.1. Electron microscopy results

Cross-sectional micrographs from the TEM studies (Fig. 6) confirm well-defined layer-structures in the W–SiO$_2$ absorber with a thickness variation of about 5–10 nm in the individual layers. This topographic variation seems to originate from the columnar growth in the Mo layer. The cermet and AR layer do not show clear columns but replicate the unevenness in the Mo columnar structure. The thickness variation of 5–10 nm has only a tiny effect on the thin film optical interference that is needed for good spectral selectivity. It is seen in Fig. 4 that the interference pattern is somewhat more pronounced in the modelled reflectance where the front surface and interfaces are optically smooth.

It is possible to only distinguish two layers on top on the Mo reflector, which is puzzling since three layers have been deposited. Fig. 7a shows the coating in higher resolution and it is not possible to distinguish three layers here either. The middle layer seems to be missing, probably because the tungsten concentration is very low and therefore not distinguishable from the AR layer. The use of energy-filtered TEM as well as STEM EDX was tried in order to detect low concentration of tungsten but this element was not possible to resolve. The total thickness of middle and AR layer was 93 nm when modelled and 83 nm when sputtered (Table 2), and to be compared with the top layer thickness of 80–85 nm in Fig. 6. This implies that the base layer is the darker layer. It has a thickness of about 65–70 nm to be compared with 75 nm and 76 nm respectively in Table 2.

The magnified micrograph in Fig. 7a shows a grainy structure with darker spots having traces of parallel planes of only a few nm in size. It indicates a nano-range order but not as clear as for well-defined distinct nano-particles. In Fig. 7b it is possible to observe areas of sharper parallel planes indicating crystal order of about
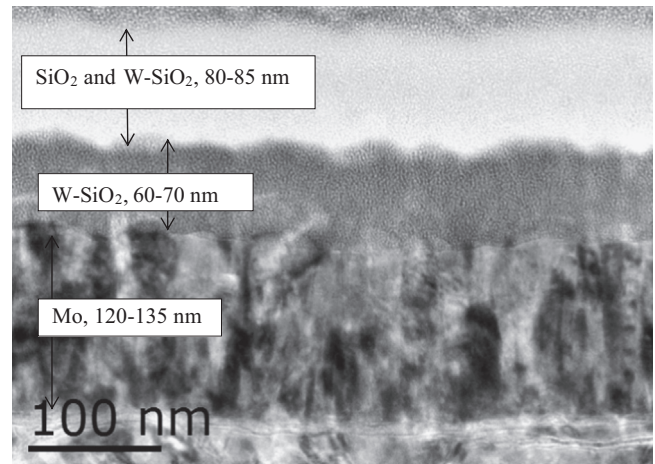

Fig. 6. TEM micrograph in cross-sectional view of W–SiO$_2$ absorber coating.

5 nm in size which could be W particles. This will be disussed more in Section 3.2.3.

Fig. 8 shows the cross-sectional TEM micrograph of Nb–TiO$_2$ absorber and in this coating it is possible to distinguish the middle and base cermet layers, where the latter appears darker than the former. According to the modelled coating in Table 2 the volume fraction is rather high, 0.25 in the middle layer and should therefore be distinguishable from the pure AR SiO$_2$ layer. The thicknesses of the three layers are base layer 15–20 nm, middle layer 60–65 nm and AR layer 70–80 nm. The TEM micrograph is not from the same samples as in Table 2 but from samples with similar optical performance (α_{sol} and ε_T). The AR layer has about the same thickness in both samples. The middle layer is thinner in the sample presented in Table 2, which is a compensation for a thicker base layer. The thickness of base and middle layer together is 73 nm (from deposition rates and times) for the sample in Table 2 compared to 75–85 nm in the TEM sample.

The high-resolution micrographs in Fig. 9 for Nb–TiO$_2$ shows areas with parallel lines indicating particles of the size 10 nm in the cermet layer (Fig. 9b). The particles are more distinct than in the W–SiO$_2$ cermet. The structure in the AR SiO$_2$ layer is similar to the one shown in Fig. 7a, which is reasonable as they are produced with similar conditions in the same sputtering unit.

3.2.2. AES results

The spectra shown in Fig. 10 represent the W_{NNN} line shapes of pure metallic (a) and oxidized (b) W. The tungsten Auger transition of a cermet base layer of W–SiO$_2$ is shown in (c). The triplet observed at 163, 169 and 179 eV (a, c) is characteristic of a W elemental state; these peaks are replaced by a doublet at 163 and 175 eV and a small shoulder at 158 eV if the W is in oxidized state.
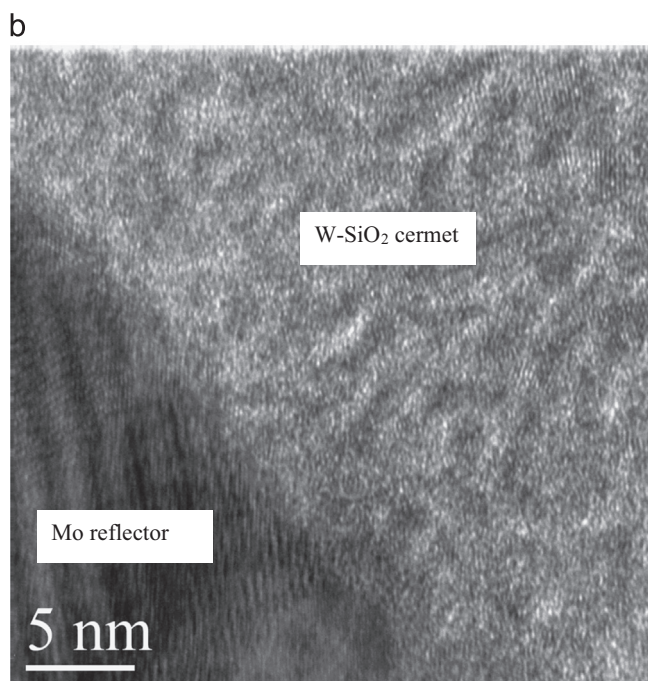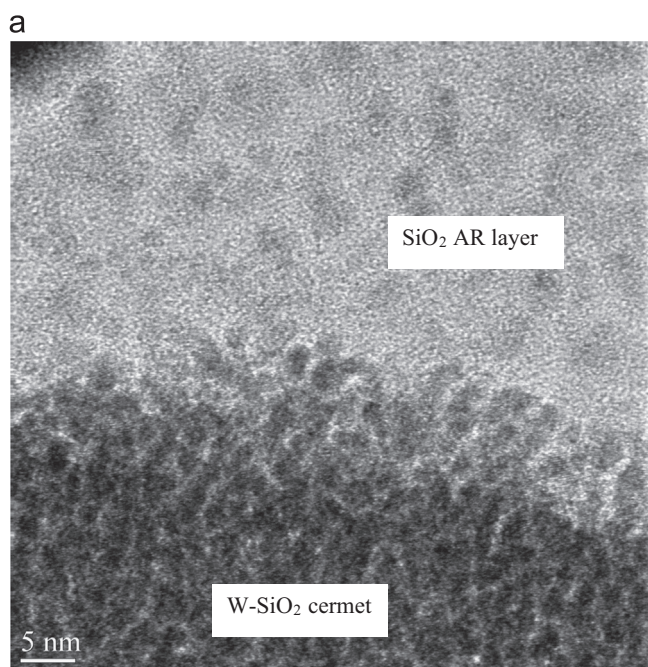
a

SiO₂ AR layer

W-SiO₂ cermet

5 nm

b

W-SiO₂ cermet

Mo reflector

5 nm

Fig. 7. TEM micrographs, cross-sectional view, displaying in more detail the structure in each layer of the W–SiO₂ coating.

Hence, the Auger line shapes of W in the cermet layer can be unambiguously assigned to the spectra of W in pure metal. This means that we can identify tungsten to be in the metallic phase [20].

Fig. 11c shows the niobium spectra acquired on the Nb–TiO₂ cermet base layer. The Nb$_{MNN}$ transition at 167 eV (see Fig. 11a) is characteristic for metallic niobium (Nb°) [21]. A shoulder occurring at about 5 eV at the left energy side of the peak can be assigned to oxidized Nb (see Fig. 11b). This latter structure is attributed to the electron transfer from Nb (4d) valence band to O (2p) [22]. Smaller energy shift (< 5 eV) can be correlated to lower niobium oxidation states, i.e. Nb^{2+} and Nb^{4+} [22]. The small energy shift (2 eV) measured for the MNN transition can be due to a small charging

SiO₂, 70-80 nm

Nb-TiO₂, 60-65 nm

Nb-TiO₂, 15-20 nm
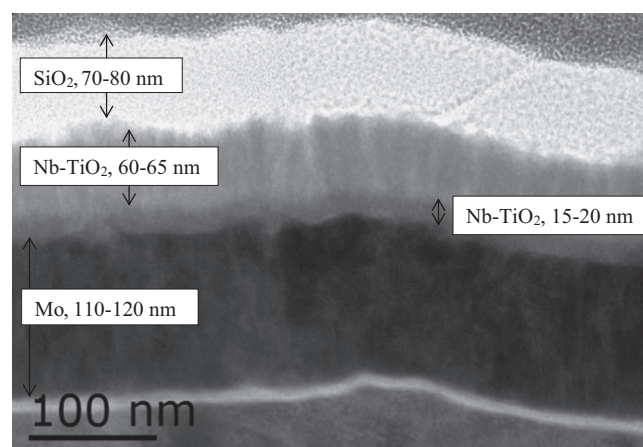
Mo, 110-120 nm

100 nm

Fig. 8. TEM micrograph in cross-sectional view of Nb–TiO₂ absorber coating.

effect on the sample surface. It can be concluded from the Nb$_{MNN}$ Auger line analysis that the main part of Nb is in metallic phase.

3.2.3. XRD results

The diffractograms for the base layers of the two cermets, W–SiO₂ and Nb–TiO₂ are presented in Figs. 12a and 12b respectively. A broad peak, centred at 23° is seen on both samples. This is due to the diffraction from the amorphous glass substrate as this broad peak also exists on a pure substrate. On the W–SiO₂ cermet there are two distinct peaks, one at 40° and a less intense, broader peak at 70°, due to different tungsten crystal planes. Also shown in Fig. 12a is the diffractogram for a pure tungsten film sputtered under similar conditions as the cermet layer. This shows good agreement with reference data for tungsten [23]. The AES data (Fig. 10a) indicates no detectable level of oxidized states and then supports mainly metallic tungsten in the cermet.

For the TiO₂–Nb cermet film a sharp peak is seen at 36° with a distinct shoulder at 39°. The main peak, which is narrower compared to the tungsten peak in Fig. 12a, is due to diffraction from niobium crystal planes, as evidence from the measurement on a pure sputtered niobium film, Fig. 12b. This does not fully correspond to the tabulated data where the bcc [110] planes in niobium is seen between 38° and 39° [23]. The discrepancy in the diffractogram for sputtered niobium and the tabulated reference data can possible be due to structural differences in the nano-sized particles compared to data for poly or single crystal materials. It can also be influenced by formation of oxidized states as was found from AES (Fig. 10b). For TiO₂ no clear peaks are seen either in the cermet layer film or in the pure TiO₂ film, which suggest that the sputtered TiO₂ is amorphous.

Hence combining these results with the findings from TEM and AES it indicates that W is found in a metallic phase inside the matrix with a particle size of around 5 nm. In the Nb–TiO₂ cermet the larger crystal grains observed in the micrographs (Fig. 9b) are due to Nb particles, possible with a minor oxidation, and a particle size about 10 nm. The larger size for Nb particles found it TEM supports the narrower Nb diffraction peak indicating also larger particles in comparison with W.

3.2.4. ERDA

The concentrations of all detectable elements in the W–SiO₂ absorber are presented in Fig. 13 where they are plotted together with the TEM cross sectional micrograph scaled to make it more convenient to identify the different sub-layers. As can be seen the element signals are smeared out considerable in the ERDA
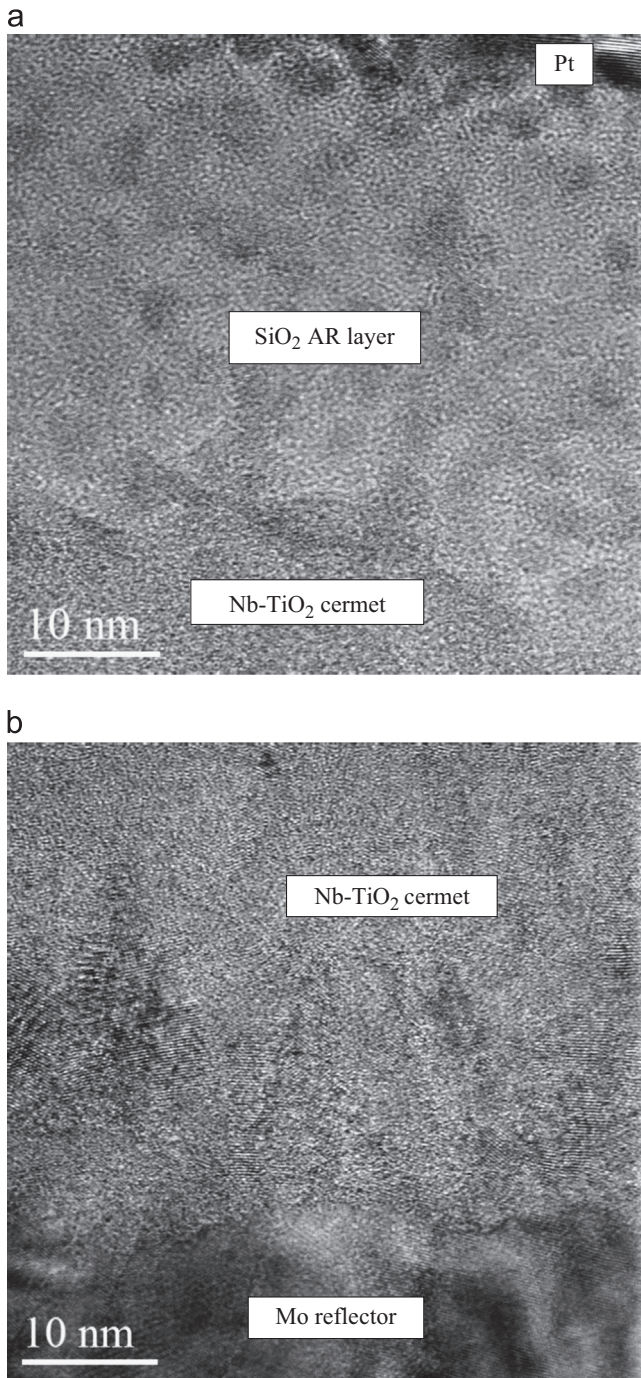
a

b

Fig. 9. TEM micrographs, cross-sectional view, in more detail the structure in each layer of the Nb–TiO$_2$ coating.

Fig. 10. Auger NNN transition for pure metallic W (a), oxidized W (b) and for one cermet base layer of W–SiO$_2$ (c).

Fig. 11. Auger MNN transition for pure metallic Nb (a), oxidized Nb (b) and for one cermet base layer of Nb–TiO$_2$ after 1 min of sputtering (c).

recording. The AR layer shows a ratio for silicon to oxygen of 1–2. Also tungsten can be observed in this layer as a long tail from the higher concentration in the base layer. While a low concentration of W in the AR layer can thus not be totally excluded it can be attributed mostly to energy loss straggling, and the rather large size of the analysis spot (2 mm^2) due to which possible small variations in film thickness on this rather large lateral length scales can contribute. Due to the same reasons W from the base layer is also detected on the depth level of the middle layer. The W element concentration estimated in the base layer gives roughly half the value as for Si in the same layer. Assuming stoichiometric silica (i.e. a ratio of 1–2 for Si to O) also in the cermet we can make a rough estimation that tungsten to silica is about 1–2 in ratio. The
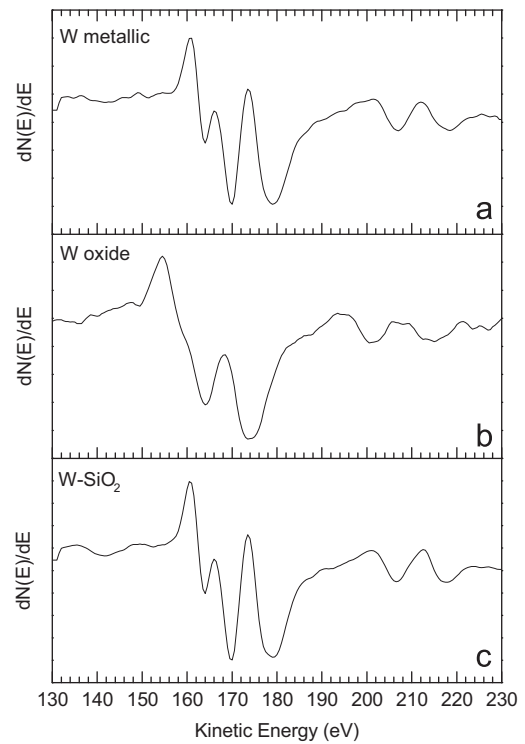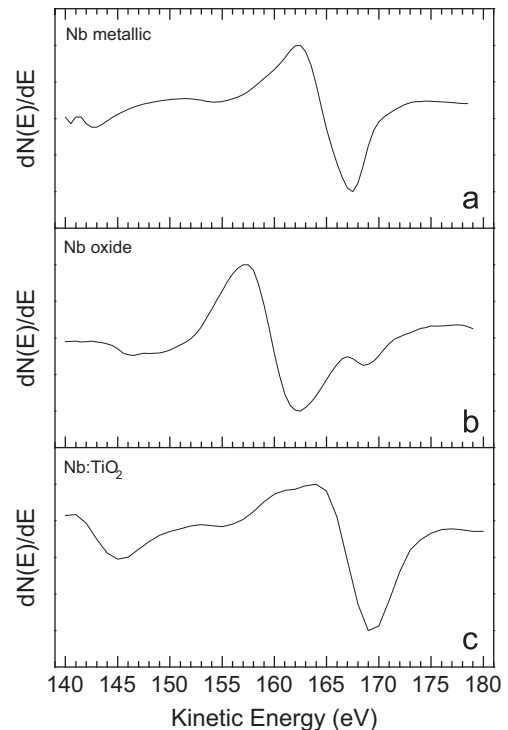
molecule SiO$_2$ has a slightly smaller volume per unit cell than W but still in a rough estimate a ratio of 1–2 holds also for volume concentrations W to SiO$_2$. Comparing with the volume fractions in Table 2, with a theoretical volume fraction of 0.33 the real cermet seems to have roughly the same volume concentration.
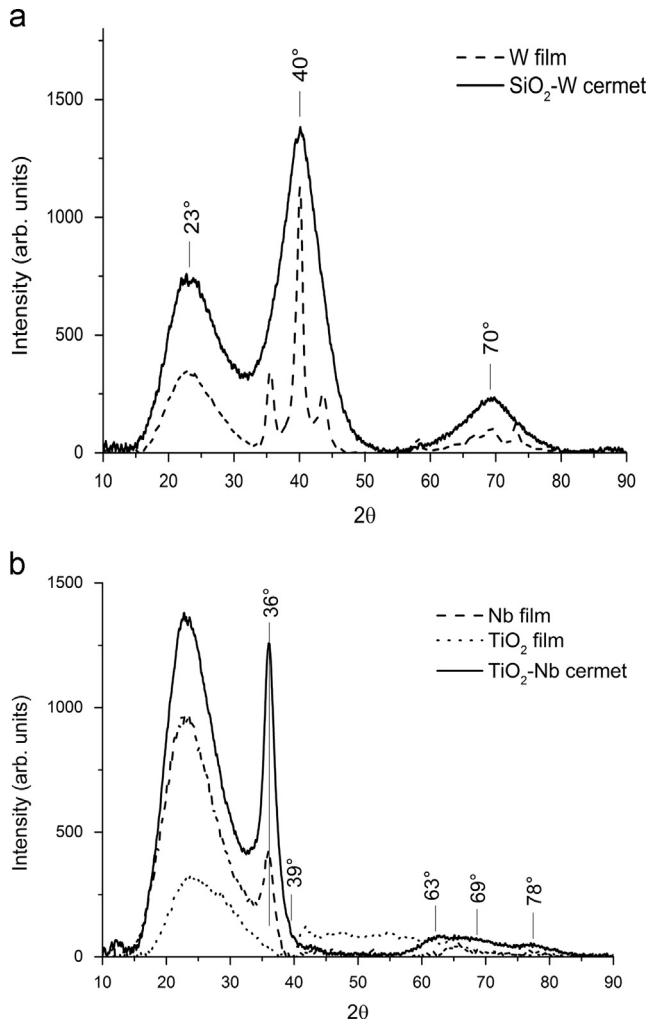
Fig. 12. (a) W–SiO$_2$ base layer on glass substrate. Bragg reflection for W is indicated (b) Nb–TiO$_2$ base layer on glass substrate. Bragg reflection for Nb is indicated.

Fig. 13. ERDA depth resolved yields for W–SiO$_2$ combined TEM cross-sectional view.

Fig. 14. ERDA depth resolved yields for Nb–TiO$_2$ absorber coating. Notify that Nb in the cermet and Mo infrared reflector were not possible to separate, and both are marked as "Mo/Nb".

ERDA results for Nb–TiO$_2$ are presented in Fig. 14. The AR layer is easier to distinguish from the cermet layers thus it is not necessary to show a TEM micrograph in this case. However, one experimental problem is that Nb and Mo are too close in atomic weight and they were thus not possible to resolve. The Nb content represents the left side shoulder in the joint curve for Nb and Mo. It is therefore not possible to estimate the Nb content in a similar way as done above for W. The AR layer shows also for this absorber a ratio for silicon to oxygen of about 1–2, which is expected since this layer is produced in the same way as for the W–SiO$_2$ absorber.

Except for the expected elements in substrate and coatings, they are also contaminated with hydrogen and carbon. The carbon is on an average level of 0.006 in the interior of the stainless steel substrate. In comparison, the C content is found lower in the W–SiO$_2$ coating (0.003) but considerable higher in the Nb–TiO$_2$ cermets (0.02–004). Hydrogen is present in both types of coatings, in a higher concentration in Nb–TiO$_2$, on an average level of 0.03 and about 0.02 on average in the W–SiO$_2$ absorber. There is a constant ratio of hydrogen to carbon in the Nb–TiO$_2$ sample both in the cermet coatings and the AR coating that could indicate hydrocarbon constituents. This is not the case in W–SiO$_2$, which then could be interpreted by the fact that the hydrogen is in this case preferably bound in hydroxide complexes. The differences regarding the contaminations are probably an effect of the use of different sputtering units and sample handling in connection to this. Worth to mention is also the iron contamination in the
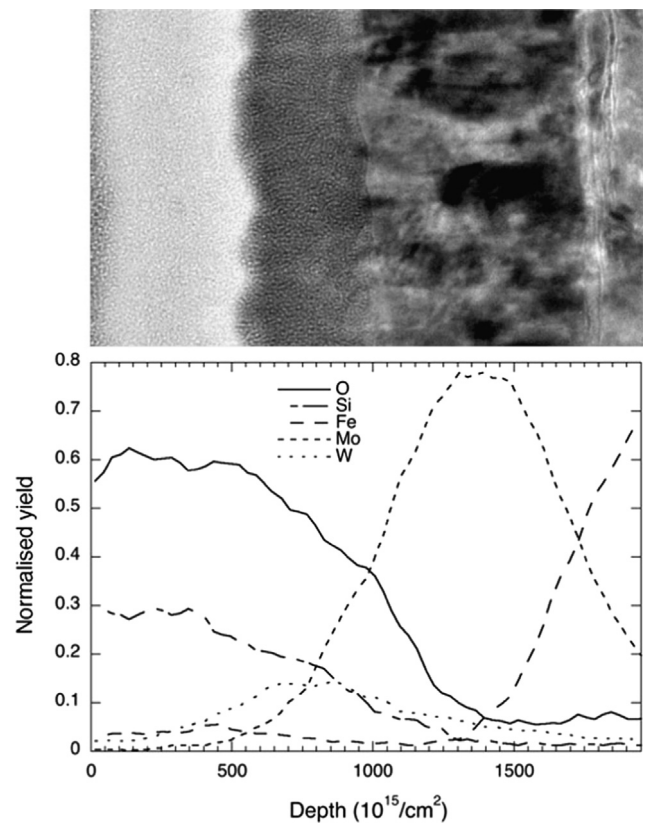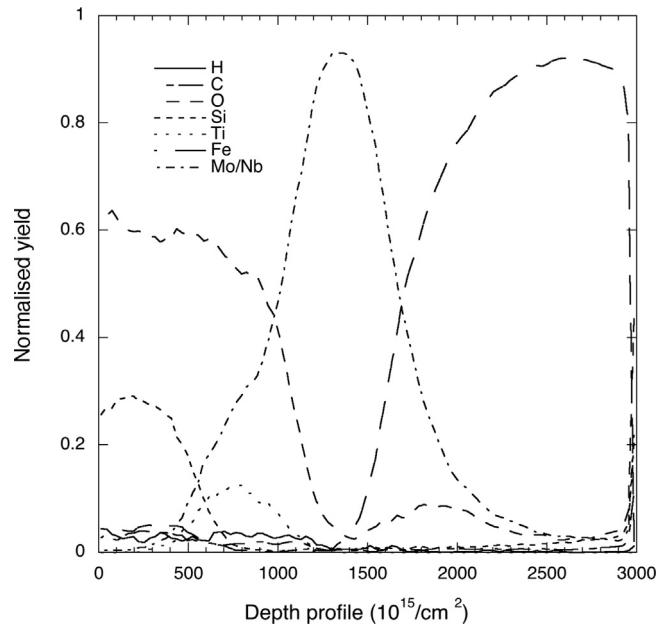
coatings. It is present in all layers in the W–SiO$_2$ absorber, while in Nb–TiO$_2$ absorber it is only detected in the AR layer. The contamination is an effect of rf sputtering in the unit at The Ångström Laboratory, where the steel chamber walls are to some extent sputtered and incorporated in the produced coatings. This has not been a problem in the FBK sputtering unit.
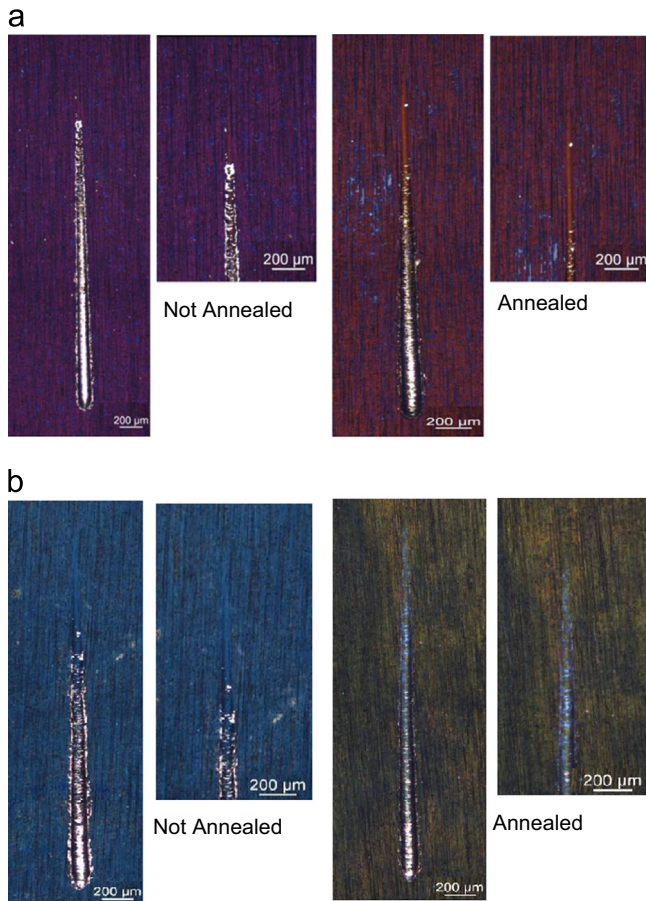
Fig. 15. Scratches performed before and after annealing at 350 °C in vacuum on (a) W–SiO$_2$ and (b) Nb–TiO$_2$.

Table 4
Results from temperature test at 350 °C in vacuum. Recorded changes in solar absorptance (α_{sol}) and thermal emittance at 350 °C (ε_{350}).

Sample	α before	α after	$\Delta\alpha$	ε_{350} before	ε_{350} after	$\Delta\varepsilon_{350}$	Time (h)
SiO$_2$/W–SiO$_2$/Mo/SS	0.92	0.92	0.00	0.11	0.07	0.04	1531
SiO$_2$/W–SiO$_2$/Mo/SS	0.91	0.91	0.00	0.08	0.07	0.01	144
SiO$_2$/Nb–TiO$_2$/Mo/SS	0.86	0.85	0.01	0.08	0.07	0.01	1272
SiO$_2$/Nb–TiO$_2$/Mo/SS	0.92	0.92	0.00	0.09	0.08	0.01	72

Table 3
Distances (from the scratches tips) of the first and second observed defect, normal and tangential forces and drag coefficients.

Coating	1st defect (µm)	F_N (N)	F_T (N)	Drag coeff.	2nd defect (µm)	F_N (N)	F_T (N)	Drag coeff.
W–SiO$_2$	329	3.32	0.19	0.057	461	4.64	0.35	0.075
W–SiO$_2$	297	3.00	0.16	0.053	825	8.27	0.72	0.087
Nb–TiO$_2$	636	6.39	0.32	0.050	795	7.97	0.37	0.046
Nb–TiO$_2$	786	7.88	0.47	0.060	1228	12.30	1.00	0.081

3.2.5. Scratch tests results

The scratch tests revealed that the coatings mechanical strength is generally satisfying and after annealing their behaviour seems even to improve as seen in Fig. 15.

In all the tests, two main damages should be remarked: the first one, smaller, close to the scratch tip and a second one, larger, that can be considered the beginning of the macroscopic removal of the coating, Table 3.

3.3. Durability results

The samples used in the temperature tests are not in all cases the same samples as presented in Table 2, as seen from the initial performance values in Table 4. Two samples of each cermet were tested, one with good optimal performance and the other with a worse performance.
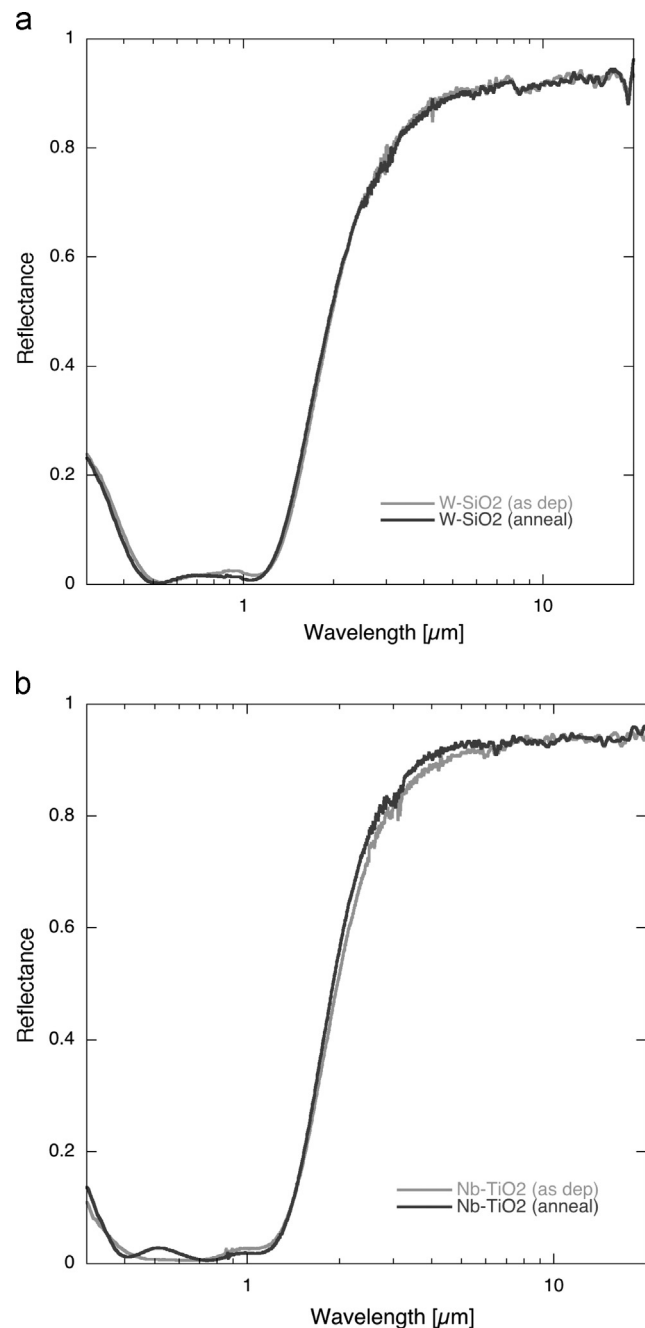

Fig. 16. The reflectance spectrum before and after annealing at 350 °C in vacuum in (a) W–SiO$_2$ for about 1500 h, (b) Nb–TiO$_2$ for 72 h.

There is a small change in reflectance after annealing that primarily influences the thin film interference pattern and implies a change in thickness and/or materials composition in at least one layer as seen in Fig. 16. The change in reflectance takes place during the first test period of 72 h, after that the values are stable.

All four samples get a positive effect of the annealing with a decreased emittance from the first 72 h exposure. This effect is pronounced in the sample with the initially high emittance.

TEM micrographs from the same samples before and after annealing show no observable differences due to the annealing and are therefore not presented here.

ERDA measurements show shifts in the peak position and change in peak heights in both absorber types for metal and silicon contents (Figs. 17a and 18a). However, it is difficult to draw any clear conclusions from these single measurements. Possibly, the differences could be due to the fact that different positions on
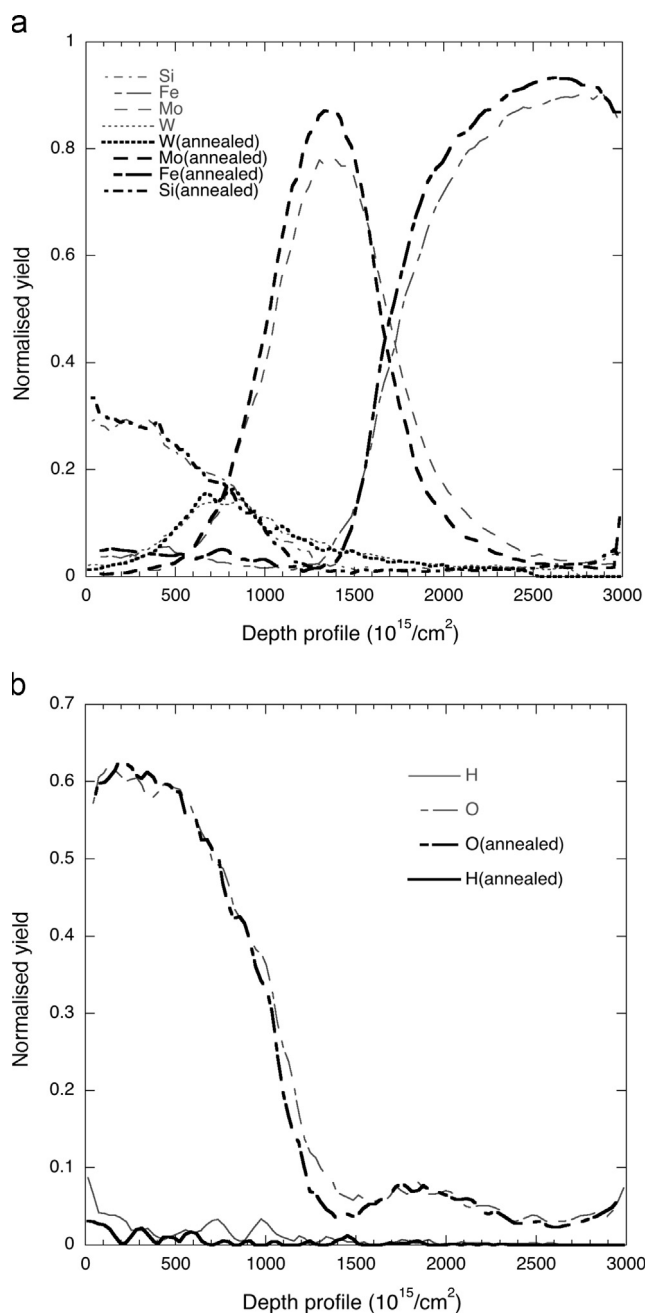

Fig. 18. Comparison of elements before and after annealing at 350 °C in vacuum in Nb–TiO$_2$ for about 1300 h (a) metal and Si contents (b) hydrogen and oxygen.

Fig. 17. Comparison of elements before and after annealing at 350 °C in vacuum in W–SiO$_2$ for about 1500 h (a) metals and Si contents (b) hydrogen and oxygen.
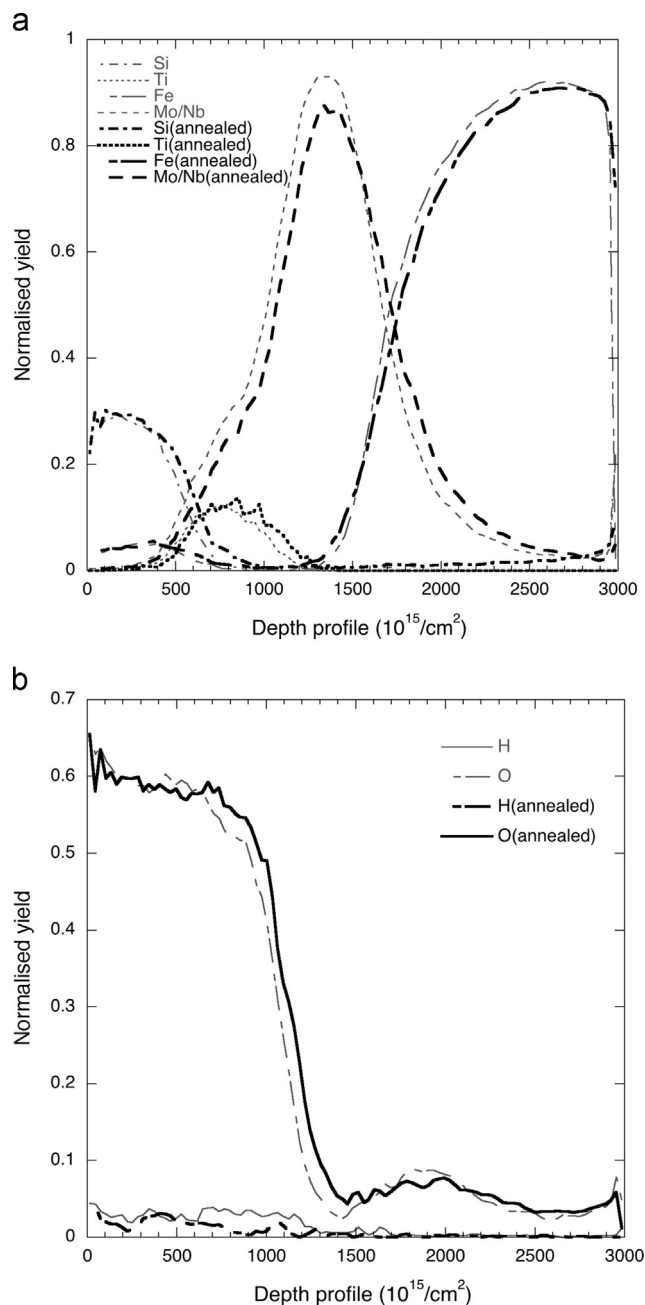
the samples have been measured before and after annealing and the changes instead reflect uneven layers thickness in the samples.

Anyhow, there seems to be a temperature dependent relative decrease in hydrogen and increase in oxygen content as seen in Figs. 17b and 18b. This could explain the small shifts in optical interference after annealing and could be a change from hydroxides to oxides in the layers with outgassing of hydrogen.

Carbon content is not changed after annealing in W–SiO$_2$ but does decrease in Nb–TiO$_2$. This supports that in Nb–TiO$_2$ hydrogen is bound in hydrocarbon compounds, which are outgassed.

A more systematic investigation must be done in order to be certain of real temperature initiated changes but the changes are very small and also have a positive effect of decreasing the emittance. It has not been of high priority in this study to investigate it further.

4. Conclusions

New absorber coatings have been developed for mid-temperature applications in the temperature range 300–400 °C. The design is based on the tandem surface concept with a three-layer stack for high solar absorption on a molybdenum infrared reflector. The three-layer stack consists of a SiO_2 antireflection layer with two cermet-layers below, a middle with low metal content and a base layer with high metal content. Two types of cermets were investigated: $W–SiO_2$ and $Nb–TiO_2$. The results show that both perform equally well as mid-temperature solar absorbers with as-prepared solar absorptance/thermal emittance (at 350 °C) of 0.91/0.08 and 0.93/0.09 respectively. The $W–SiO_2$ absorber could also be fabricated with a higher absorptance and then consequently a higher emittance and vice versa for the $Nb–TiO_2$ absorber. The goal was to achieve a solar absorptance of at least 0.93 combined with a thermal emittance at 350 °C of 0.10 or less. The reported absorptance for the $W–SiO_2$ absorber is not reaching the targeted value but it is believed that if the thermal emittance was allowed to reach 0.10 the absorptance could reach 0.93. No such samples were however prepared for this study. In order to improve these absorber coatings further, the infrared reflector must be changed to a metal with lower emittance, but then more protecting layers must be introduced as done in [3,4] where silver was replacing molybdenum. The Mo reflector used here from sputter-deposition was contributing with 0.07–0.08 by itself.

The emittance is decreased after annealing for 72 h, which improves the performance. Another positive effect is also an improved coating adhesion, although it is good enough already as prepared. Curing the absorber coating at operation temperature (or higher) should therefore be the final step in the coating preparation. Apart from an initial decrease in emittance the coatings are stable in long time testing at operation temperature.

The optimization follows two steps, starting from theoretical optimization using optical constants derived from thin films of the cermet constituents sputtered with the same conditions as the cermet and AR-layers, and then preparing the coatings using the thicknesses and volume fractions of the constituents found in the first step. It is seen that there is a good agreement between the real coatings and those modelled with optical constants of the sputtered films considering the accuracy in the determined optical constants and in the reproducibility in the sputtering process.

The sputtered oxides (SiO_2 and TiO_2) are found from TEM to consist of nano-scale order but not ordered enough to be detected with XRD. In both cases it means that such structural conditions influence the optical constants to deviate from bulk materials optical data in literature. The optical constants derived for the sputtered thin films are probably more similar to the physical properties of the cermet materials but there are still differences between nano-thin films and nano-size particles. Also the method used here to derive optical constants from thin films has its weaknesses since the causality between n and k is not taken in account.

The existence of metal particles was confirmed from AES, XRD and TEM and it means that cermet structure exists and that effective medium models, in this case Bruggeman can be used. The results indicate larger Nb particles (10 nm) and smaller W particles (5 nm). The reason for this is not known, they are produced in different sputtering units and processes but there is not enough systematic data for in the present study for indicate plausible explanations.

The present study appears in line with earlier work on cermet based absorber coatings such as $Mo–Al_2O_3$, $Mo–SiO_2$ and $W–Al_2O_2$, as referred to in the introduction about the difficulty to combine a high solar absorptance (0.95 or higher) with a very low thermal emittance at mid-temperatures (0.05 or lower). This is reached easier for similar types of absorber coatings for low-temperature applications, because the selectivity is promoted by having the solar and black body spectra are more apart in the NIR wavelength range. Also, because the absorber material of aluminium, nickel-plated copper or bare copper offers an infrared reflector with lower emittance than molybdenum that is used on steel absorber tubes. Hence, the challenge in mid-temperature applications is to improve the selectivity by making the transition from low to high reflectance as steep as possible and to find an alternative to molybdenum that does not increase complexity in the production which means as few sub-layers as possible.

References

[1] L. Crema, R. Bartali, F. Alberti, E. Wackelgard, B. Rivolta, S. Hesse, L. Luminari, D. Hislop, B. Restall, Novel m-CHP generation from small scale concentrated solar power, SHC2013, in: Proceedings of the International Conference on Solar Heating and Cooling for Buildings and Industry, September 23–25 in Freiburg. Energy Procedia, Special Issues, 2014, in preparation.

[2] M. Lanxner, Z. Elgat, Solar selective absorber coatings for high service temperatures, produced by plasma sputtering, in: Proceedings of the Society of Photo-Optical Instrumentation Engineers, vol. 1272, 1990, pp. 240–249.

[3] C. Hildebrandt, Fakultät Energie-,Verfahrens- und Biotechnik (Doctoral thesis), Universität Stuttgart, Stuttgart, 2009.

[4] A.B. Meinel, M.P. Meinel, Applied Solar Energy – An Introduction, Addison-Wesley, Reading, Massachusetts, Menlo Park, California, London, Amsterdam, Don Mills Ontario, Sydney, 1976.

[5] A. Antonaia, A. Castaldo A, M.L. Addonizio, S. Esposito, Stability of $W–Al_2O_3$ cermet based solar coating for receiver tube operating at high temperature, Sol. Energy Mater. Sol. Cells 94 (2010) 1604–1611.

[6] L. Zheng, F. Gai, S. Zhao, F. Zhou, J.P. Nshimiyimana, X. Diao, Optical design and co-sputtering preparation of high performance $Mo–SiO_2$ cermet solar selective absorbing coating, Appl. Surf. Sci. 280 (2013) 240–246.

[7] N.P. Sergeant, O. Pincon, M. Agrawal, P. Peumans, Design of wide-angle solar-selective absorbers using aperiodic metal-dielectric stacks, Opt. Express 17 (2009) 22800–22812.

[8] A.A. Shah, M.C. Gupta, Spectral selective surfaces for concentrated solar power receivers by laser sintering of tungsten micro and nano particles, Sol. Energy Mater. Sol. Cells 117 (2013) 489–493.

[9] C.E. Kennedy, Review of Mid- to High-Temperature Solar Selective Absorber Materials, NREL/TP-520-31267, National Renewable Energy Laboratory, Golden, CO, 2002.

[10] D. Chester, P. Bermel, J.D. Joannopoulos, M. Soljacic, I. Celanovic, Design of global optimization of high-efficiency solar thermal systems with tungsten cermets, Opt. Express 19 (2011) 245–257.

[11] Y. Liu, C. Wang, Y. Xue, The spectral properties and thermal stability of NbTiON solar selective absorbing coating, Sol. Energy Mater. Sol. Cells 96 (2012) 131–136.

[12] W. Theiss, Hard and Software for Optical Spectroscopy (www.mtheiss.com), Aachen, Germany, 2002.

[13] G.T. Georgiev, J.J. Butler, Long term calibration monitoring of Spectralon diffusers BRDF in the air-ultraviolet, Appl. Opt. 46 (2007) 7892–7899.

[14] Y. Zhang, H.J. Whitlow, T. Winzell, I.F. Bubb, T. Sajavaara, K. Arstila, J. Keikonen, Detection efficiency of time-of-flight energy elastic recoil detection analysis systems, Nucl. Instrum. Methods B 149 (1999) 477–489.

[15] H.J. Whitlow, G. Possnert, C.S. Petersson, Quantitative mass and energy dispersive elastic recoil spectrometry: resolution and efficiency considerations, Nucl. Instrum. Methods B 27 (1987) 448–457.

[16] T. Boström, J. Jensen, S. Valizadeh, G. Westin, E. Wäckelgård, ERDA of $Ni–Al_2O_3$/ SiO_2 solar thermal selective absorbers, Sol. Energy Mater. Sol. Cells 92 (2008) 1177–1182.

[17] M.S. Janson, CONTES (CONversion of Time-Energy Spectra) a program for ERDA data analysis, Internal report, Uppsala University, 2004.

[18] E.D. Palik, Handbook of Optical Constants of Solids, Academic Press, Orlando, 1985.

[19] J.H. Weaver, D.W. Lynch, C.G. Olson, Optical properties of Nb from 0.1 to 36.4 eV, Phys. Rev. B: Solid State **7** (1973) 4311–4318.

[20] L.E. Davis, N.C. MacDonald, P.W. Palmberg, G.E. Riach, R.E. Weber, Handbook of Auger Electron Spectroscopy (edited by Physical Electronics), 2nd ed., Eden Prierie, Minnesota, 1978.

[21] Y. Wang, X. Wei, Z. Ian, Y. Cao, R. Zhai, T. Ushikubo, K.S.S. Zhuang, An AES, UPS and HREELS study of the oxidation and reaction of Nb(110), Surf. Sci. Lett. 372 (1997) L285–L290.

[22] L. Xie, D. Wang, C. Zhung, X. Guo, T. Ushikubo, K. Wada, The preparation of and water adsorption on thin films of niobium oxide on Pt(111), Surf. Sci. 320 (1994) 62–76.

[23] International Centre for Diffraction Data, ICDD, database. Nb reference: PDF (Powder Diffraction Data) 00-035-0789 and 01-088-2330; W reference: PDF (Powder Diffraction Data) 00-004-0806 and 00-047-1319 (β-W), 2012.